when the bias increases and no state is available for tunneling. This mechanism for negative differential conductance is similar to that in a double-barrier resonance tunnel diode (26).

The CB data (Fig. 4A) does show slight deviation from the characteristics of a perfect single-dot with incomplete Coulomb gap closure. Therefore, we cannot entirely rule out the possibility of dots in series on the nanotube (27, 28). A likely mechanism for NDC in this case is resonance tunneling through multiple discrete energy levels in adjacent dots. Two energy levels of double-dots involved in resonance tunneling and NDC have been observed in two-dimensional electron gas systems (29).

The high-temperature electrical characteristics of the sample shown here represent the results obtained with three modulation-doped SWNTs (diameters of $\sim$2 nm). The modulated doping scheme reliably leads to intramolecular p^+n^+ junctions exhibiting negative differential conductance. At low temperatures, CB phenomena are consistently observed with the samples, but with the manifestation of unintentional doping modulation effects (not noticeable at high temperatures). This points to a need for much better control of the chemical homogeneity along the nanotube length. Most important, it also suggests that controlled doping modulations over a length scale of <100 nm along a nanotube should lead to well-defined quantum systems including coupled quantum dots. Modulated chemical doping of nanotubes holds promise as a new route to intramolecular devices.

References and Notes

1. W. Shockley, *IEEE Trans. Electron. Devices* ED-23, 597 (1976).
2. L. Esaki, *IEEE Trans. Electron. Devices* ED-23, 644 (1976).
3. C. Dekker, *Phys. Today* 52, 22 (May 1999).
4. F. Leonard, J. Tersoff, *Phys. Rev. Lett.* 83, 5174 (1999).
5. K. Esfarjani, A. A. Farajian, Y. Hashi, Y. Kawazoe, *Appl. Phys. Lett.* 74, 79 (1999).
6. R. D. Antonov, A. T. Johnson, *Phys. Rev. Lett.* 83, 3274 (1999).
7. L. Chico, V. H. Crespi, L. X. Benedict, S. G. Louie, M. L. Cohen, *Phys. Rev. Lett.* 76, 971 (1996).
8. J. Hu, M. Ouyang, P. Yang, C. M. Lieber, *Nature* 399, 48 (1999).
9. Z. Yao, H. W. C. Postma, L. Balents, C. Dekker, *Nature* 402, 273 (1999).
10. J. Kong, H. Soh, A. Cassell, C. F. Quate, H. Dai, *Nature* 395, 878 (1998).
11. S. Tans, A. Verschueren, C. Dekker, *Nature* 393, 49 (1998).
12. R. Martel, T. Schmidt, H. R. Shea, T. Hertel, P. Avouris, *Appl. Phys. Lett.* 73, 2447 (1998).
13. C. Zhou, J. Kong, H. Dai, *Appl. Phys. Lett.* 76, 1597 (1999).
14. P. G. Collins, K. Bradley, M. Ishigami, A. Zettl, *Science* 287, 1801 (2000).
15. J. Kong et al., *Science* 287, 622 (2000).
16. J. Kong, C. Zhou, E. Yenilmez, H. Dai, *Appl. Phys. Lett.*, in press.
17. R. S. Lee et al., *Phys. Rev. B* 61, 4526 (2000).
18. M. Bockrath et al., *Phys. Rev. B* 61, R10606 (2000).
19. B. G. Streetman, *Solid State Electronic Devices* (Prentice-Hall, Englewood Cliffs, NJ, 1995).
20. H. Grabert, M. H. Devoret, Eds., *Single Charge Tunneling* (Plenum, New York, 1992).
21. S. J. Tans et al., *Nature* 386, 474 (1997).
22. M. Bockrath et al., *Science* 275, 1922 (1997).
23. J. Nygard, D. H. Cobden, M. Bockrath, P. L. McEuen, P. E. Lindelof, *Appl. Phys. A* 69, 297 (1999).
24. A. Bachtold et al., *Phys. Rev. Lett.* 84, 6082 (2000).
25. S. Tans, C. Dekker, *Nature* 404, 834 (2000).
26. L. L. Chang, L. Esaki, R. Tsu, *Appl. Phys. Lett.* 24, 593 (1974).
27. A. Bezryadin, A. Verschueren, S. Tans, C. Dekker, *Phys. Rev. Lett.* 80, 4036 (1998).
28. P. L. McEuen, M. Bockrath, D. H. Cobden, Y.-G. Yoon, S. G. Louie, *Phys. Rev. Lett.* 83, 5098 (1999).
29. N. C. vander Vaart, S. F. Godijn, Y. V. Nazarov, C. J. P. M. Harmans, J. E. Mooji, *Phys. Rev. Lett.* 74, 4702 (1995).
30. Supported by the National Science Foundation, Defense Advanced Research Projects Agency/Office of Naval Research, Semiconductor Research Corporation/Motorola, a David and Lucile Packard Fellowship, a Terman Fellowship, the Laboratory for Advanced Materials at Stanford, National Nanofabrication Users Network at Stanford, the Camile Henry-Dreyfus Foundation, and the American Chemical Society.

Powering an Inorganic Nanodevice with a Biomolecular Motor

Ricky K. Soong,[1,2] George D. Bachand,[1,2] Hercules P. Neves,[1,2] Anatoli G. Olkhovets,[1,3] Harold G. Craighead,[1,3] Carlo D. Montemagno[1,2]*

Biomolecular motors such as F_1–adenosine triphosphate synthase (F_1-ATPase) and myosin are similar in size, and they generate forces compatible with currently producible nanoengineered structures. We have engineered individual biomolecular motors and nanoscale inorganic systems, and we describe their integration in a hybrid nanomechanical device powered by a biomolecular motor. The device consisted of three components: an engineered substrate, an F_1-ATPase biomolecular motor, and fabricated nanopropellers. Rotation of the nanopropeller was initiated with 2 mM adenosine triphosphate and inhibited by sodium azide.

Emergent fabrication techniques permit the construction of structures with features smaller than 7 nm (1–4). However, the construction of functional nanoelectromechanical systems (NEMS) is hindered by the inability to provide locomotive forces to power NEMS devices. The use of biomolecular motors such as enzymes offers an interesting alternative to silicon-based systems (5, 6). A number of enzymes such as kinesin (7, 8), RNA polymerase (9), myosin (10), and adenosine triphosphate (ATP) synthase (5, 6, 11, 12) function as nanoscale linear or rotary biological motors. The integration of biomolecular motors with nanoscale engineered systems enables the development of hybrid organic-inorganic devices capable of using ATP as an energy source. This approach may enable the creation of a new class of sensors, mechanical force transducers, and actuators.

The F_1-ATPase enzyme, which hydrolyzes ATP in living systems, is an excellent candidate for integration with NEMS for construction of rotary biomolecular motor–powered nanodevices (5, 6). The F_1-ATPase molecule, $\sim$8 nm in diameter and 14 nm in

length, is capable of producing $\sim$80 to 100 pN·nm of rotary torque (11, 12). These characteristics of F_1-ATPase are compatible with the sizes and force constants of currently producible nanomechanical structures (5, 6). In addition, genetic modification of the F_1-ATPase sequence and structure has been used to precisely position individual F_1-ATPase molecules on engineered nanofabricated substrates (13). Previous studies have shown that actin filaments (5 nm in diameter and 1 to 4 μm in length) can be attached to the motor using biochemical techniques, and the resulting rotary motion can be visualized (11, 12). The integration of F_1-ATPase motors and nanofabricated mechanical systems, however, presents considerable engineering challenges with regard to the organic and inorganic interface (e.g., attachment chemistries, adhesion forces, and materials compatibility).

Our biomolecular motor–powered NEMS device consisted of three primary elements: (i) engineered, nanofabricated substrates of nickel (Ni) posts; (ii) recombinant F_1-ATPase biomolecular motors specifically engineered to selectively interface with nanofabricated structures; and (iii) engineered nanopropellers (Fig. 1). These elements were integrated into a functional unit using sequential attachment chemistries. Recombinant F_1-ATPase biomolecular motors were biotinylated immediately after purification and were then attached to the Ni posts using 10X histidine

[1]Nanobiotechnology Center, [2]Department of Agricultural and Biological Engineering, [3]School of Applied and Engineering Physics, Cornell University, Ithaca, NY 14853, USA.

*To whom correspondence should be addressed. E-mail: cdm11@cornell.edu

1555

tags engineered into the β-subunit coding sequence (5, 6). Streptavidin was then bound to the biotin residue on the γ subunit tip. Ni nanopropellers coated with biotinylated histidine-rich peptides were attached to the bound F_1-ATPase motors through a biotin-streptavidin linkage.

A thermostable F_1-ATPase from Bacillus PS3 was cloned, modified, and purified as described (5, 6, 14). The recombinant F_1-ATPase was labeled with biotin maleimide using an engineered unique cysteine residue on the γ subunit. The activity of the enzyme was determined using an ATP regeneration assay (11, 15).

Engineered, nanofabricated substrates were constructed as the base for the device and for attachment of biomolecular motors. Ni posts (50 to 120 nm in diameter and 200 nm high) were fabricated to prevent problems associated with increased drag on propellers due to the close proximity to the base surface. Precleaned round glass cover slips (25 mm) were coated with silicon dioxide (SiO_2) using plasma-enhanced chemical vapor deposition and were then coated with 4% polymethyl methacrylate (PMMA). A thin gold conductive layer was thermally evaporated onto the resist-coated slide for electron-beam (e-beam) lithography. The exposure pattern written onto the cover slip consisted of dots with a 2.5- or 5-μm horizontal and vertical pitch and a series of border marks to identify the post region (16). The average post measured 50 to 120 nm in diameter, depending on the e-beam exposure dose. Slides were etched with potassium iodine for removal of gold and were then immersed in methyl isobutyl ketone: isopropanol (MIBK:IPA) to develop the features. Electron gun evaporation was used to form the Ni caps on the posts. The surrounding PMMA and residual Ni were removed using acetone and methylene chloride. The posts were formed by etching the SiO_2 layer to the appropriate height with the use of a plasma-induced reactive ion etch process.

The propeller dimensions were optimized for both optical detection and minimal friction during rotation. The propellers (150 nm in diameter and 750 to 1400 nm long) were fabricated on PMMA-coated silicon wafers using e-beam lithography, and features were then developed with MIBK:IPA (17). Electron gun evaporation was used to deposit Ni for formation of the propellers; residual PMMA and Ni were removed with methylene chloride and acetone. After isotropic etching with 60% KOH to remove the propellers, the etchant was removed by dialysis and the propellers were collected by centrifugation at 500,000g for 15 min and resuspended in 1× phosphate-buffered saline (PBS). The propellers were then coated with a biotinylated His-rich peptide (NH₂-CGGSGGSHHHHHH-COOH, where C = Cys, G = Gly, H = His,

and S = Ser) to facilitate attachment to the γ subunit of F_1-ATPase, then dialyzed to remove extraneous peptide and biotin (18).

The functional device was constructed by ordered, sequential addition of the individual components. A 100-μl aliquot of biotinylated F_1-ATPase biomolecular motors (1 mg/ml in 10 mM phosphate buffer, pH 7.0) was placed directly on the engineered Ni substrates. The F_1-ATPase molecules were allowed to diffuse and bind to the Ni for 15 to 30 min. Substrates were washed three times with Buffer A [10 mM MOPS-KOH (pH 7.0), 50 mM KCl, 5 mM MgCl₂, and bovine serum albumin (10 mg/ml)]. A 100-μl aliquot of streptavidin (50 μg/ml diluted in Buffer A) was placed on the substrate and incubated for 15 min, followed by three washes with Buffer A. Finally, a 100-μl aliquot of the peptide-labeled nanopropellers was placed on the substrate and incubated for 15 to 30 min. The substrate was washed three times with Buffer A and mounted in a custom-fabricated flow cell.

Observations of propeller rotation were made using 100× oil immersion or 60× water immersion and were captured using a charge-coupled device (CCD) video camera. Buffer A was used to fill the flow cell containing the device until the patterned array (i.e., alignment marks) was located, at which time the buffer was replaced with Buffer A plus 2 mM Na₂ATP. To demonstrate the rotation dependency of the propeller, we added 10 mM sodium azide (NaN₃) to the flow cell to inhibit the activity of the F_1-ATPase motor. Rotation of propellers in the absence

of ATP (i.e., Buffer A alone) also was examined to demonstrate the functional dependency of the device on the F_1-ATPase biomolecular motor.

Of about 400 total propellers, five rotated continuously in an anticlockwise direction (Fig. 2). Rotating propellers were generally attached at a point 1/4 to 1/3 of the total propeller length from the end of the propeller, but did not show any preferential point of attachment. The majority (~80%) of the nonrotating propellers did not display any Brownian fluctuation; this suggests that the propellers either were attached to more than one F_1-ATPase motor or were bound to the motor as well as the substrate. However, it is highly unlikely that the propellers (750 nm long) were attached to multiple motors, because of the spacing (≥2.5 μm) of the Ni posts.

The rotational velocity of the device varied considerably from 0.74 to 8.3 revolutions per second (rps), with a mean velocity of 4.8 ± 0.8 rps (Fig. 3). Variation in angular velocity was caused by different lengths of the nanopropellers used in various experiments. Detailed analysis of two propellers of differing lengths revealed two distinct rotational velocities, depending on the point of attachment and length of the propeller (Fig. 3). The mean rotation velocity of rods that were 750 and 1400 nm long was 8.0 ± 0.4 and 1.1 ± 0.1 rps, respectively. Momentary pauses were occasionally observed during rotation. Backward steps and teetering between catalytic sites have been reported previously (9, 10), but were not observed during these experiments. The absence of these backward steps may be due to the maintenance
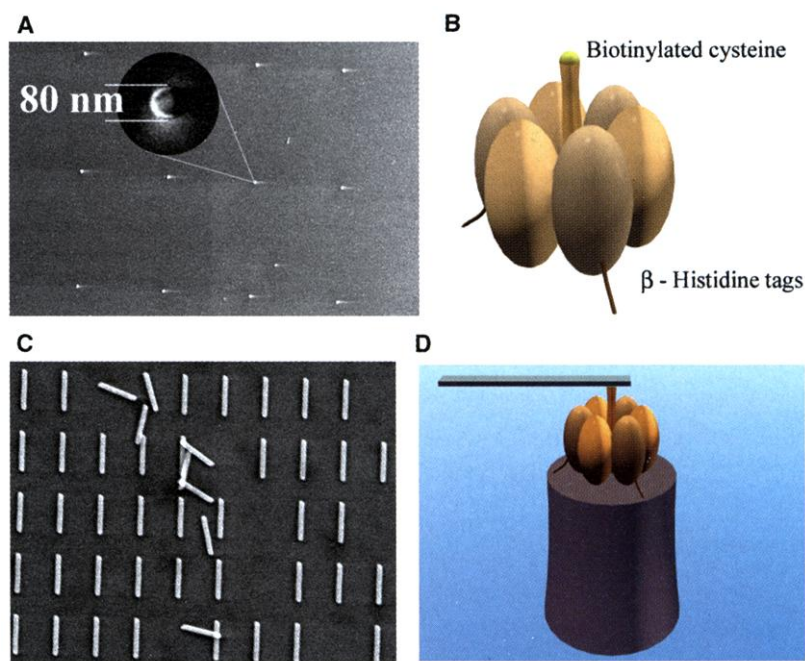
Fig. 1. Schematic diagram of the F_1-ATPase biomolecular motor–powered nanomechanical device. The device consisted of (A) a Ni post (height 200 nm, diameter 80 nm), (B) the F_1-ATPase biomolecular motor, and (C) a nanopropeller (length 750 to 1400 nm, diameter 150 nm). The device (D) was assembled using sequential additions of individual components and differential attachment chemistries.

of a high ATP concentration in the chamber; during the course of all experiments, the ATP solution was replaced every 10 min to provide a continuous fuel supply for the motor.

About 2 hours after the initial infusion of ATP into the chamber, the first rotating propeller was located and data collection began. Data were recorded for 30 min, until the propeller broke away from the motor. This result suggests that the device was functional for 2.5 hours during the first experiment, assuming that rotation began immediately upon initial infusion of ATP. Observations of other propeller–molecular motor assemblies confirmed the long life of this construct and are longer-lived than those previously reported with actin filaments (11, 12).

The addition of 2 mM ATP and 10 mM NaN₃ caused the device to cease rotation, hence the rotation of the propellers was due to F_1-ATPase motors. The difference between the rotation rates with and without NaN₃ was significant ($P < 0.01$, Mann-Whitney rank sum test). Previously rotating propellers fluctuated because of Brownian forces, but they did not rotate consistently ($<0.3 \pm 0.01$ rps) as they had before the

addition of NaN₃. Rotation was also not observed in the absence of ATP.

Because the exact dimensions of the propeller, post, and motor are known, the work done by the F_1-ATPase motor was accurately determined. The drag force per unit length for a propeller moving near a surface was calculated as

$$dF/dL = \frac{4\pi\mu U}{\cosh^{-1}(h/r)} \qquad (1)$$

(19), where h is the height of the cylinder axis relative to the surface (200 nm), U is the linear velocity, r is half the width of the propeller (75 nm), and μ is the viscosity of the medium (10^{-3} N·m s^{-2}). For small h, most energy dissipation happens in the propeller-substrate gap (20), so we can approximate the total drag by the sum of the drag forces on small segments of the propeller. The total drag torque τ is calculated by the integration along the length of the propeller

$$\tau = \frac{4}{3} \frac{\pi\mu\omega(L_1{}^3 + L_2{}^3)}{\cosh^{-1}(h/r)} \qquad (2)$$

where ω is the rotational velocity and L_1 and L_2 are the lengths of the propellers extending

from the rotational axis.

The calculated total torque on the motor was ~20 pN·nm for the 750-nm propellers (mean rotational velocity of 8.00 rps, attached ~200 nm from the end) and 19 pN·nm for the 1400-nm propellers (mean rotational velocity of 1.1 rps, attached ~350 nm from the end). The energy used ($E = 2\pi\tau$) to complete one revolution of the propellers was 119 to 125 pN·nm. About 240 pN·nm of energy is released by hydrolysis of three ATP molecules, assuming −12 kcal/mol ATP under physiological conditions (21). Thus, the measured efficiency of the motor is ~50%. However, the free energy of ATP hydrolysis depends on the concentration of Mg^{2+} and Ca^{2+} in solution, and has been reported as −7.3 kcal/mol (21) or ~150 pN·nm, giving a measured efficiency of ~80%. These energy and efficiency values are in contrast to previous reports of 100% efficiency by F_1-ATPase from Bacillus PS3, Escherichia coli, and spinach chloroplasts (11, 22–24). The values of 100% efficiency for the various F_1-ATPase types also were calculated on the basis of −12 kcal/mol ATP. The efficiency values reported here are based on more accurate estimates of the propeller length compared to the actin filaments, as well as an empirical accounting of the vertical position of the propeller with respect to the surface. Out-of-plane wobble and drag associated with the close proximity of the propeller to the top of the post may account for additional torque placed on the motor, but these phenomena are relatively insignificant with respect to the overall torque.

Our experiments demonstrate the ability to integrate biomolecular motors with nano-engineered systems to produce functional nanomechanical devices. Manipulation of individual components and attachment chemistries should help to refine the construction of these devices and improve the complexity of devices, as well as increase the efficiency and success of the assembly process.
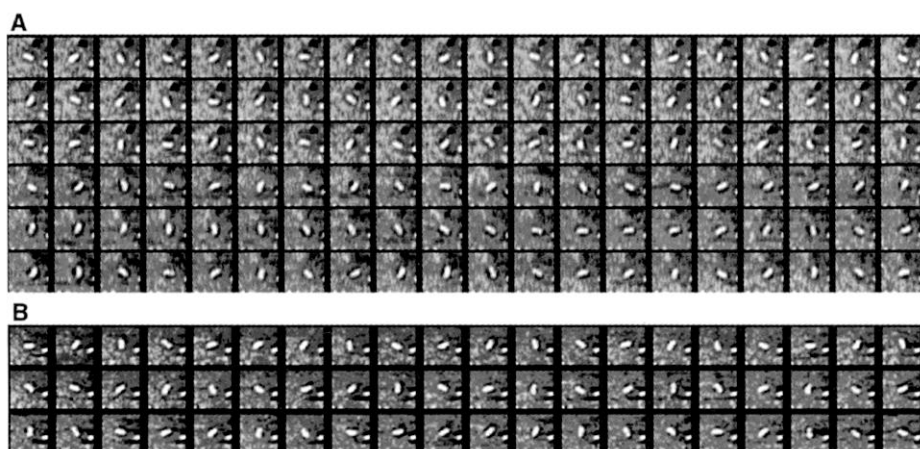
Fig. 2. Image sequence (viewed left to right) of nanopropellers being rotated anticlockwise at 8.3 rps (**A**) and 7.7 rps (**B**) by the F_1-ATPase biomolecular motor. Observations were made using 100× oil immersion or 60× water immersion and were captured with a CCD video camera (frame rate 30 Hz). The rotational velocity ranged from ~0.8 to 8.3 rps, depending on propeller length. Data were recorded for up to 30 min; however, propellers rotated for almost 2.5 hours while ATP was maintained in the flow cell. These sequences can be viewed as movies at the Nanoscale Biological Engineering and Transport Group Web site (http://falcon.aben.cornell.edu/News2.htm).

Fig. 3. Time course of F_1-ATPase γ subunit rotation. Each line represents data from a rotating nanopropeller. Solid lines, propellers 750 nm long; dashed lines, propellers 1400 nm long; dotted lines, propellers 1400 nm long in the presence of NaN₃.
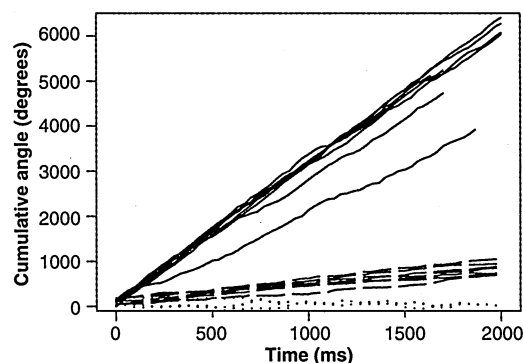
References and Notes

1. R. B. Marcus, T. S. Ravi, T. Gmitter, *Appl. Phys. Lett.* **56**, 236 (1990).
2. J. Sone *et al., Nanotechnology* **10**, 135 (1999).
3. D. W. Carr, L. Sekaric, H. G. Craighead, *J. Vac. Sci. Technol. B* **16**, 3821 (1998).
4. D. W. Carr, S. Evoy, L. Sekaric, J. M. Parpia, H. G. Craighead, *Appl. Phys. Lett.* **75**, 920 (1999).
5. C. D. Montemagno, G. D. Bachand, *Nanotechnology* **10**, 225 (1999).
6. G. D. Bachand, C. D. Montemagno, *Biomed. Microdevices* **2**, 179 (2000).
7. S. M. Block, *Cell* **93**, 5 (1998).
8. M. J. Schnitzer, S. M. Block, *Nature* **388**, 386 (1997).
9. M. Wang *et al., Science* **282**, 902 (1998).
10. K. Kitamura, M. Tokunaga, A. H. Iwane, T. Yanagida, *Nature* **397**, 129 (1999).
11. R. Yasuda, H. Noji, K. Kinosita Jr., M. Yoshida, *Cell* **93**, 1117 (1998).
12. H. Noji, R. Yasuda, M. Yoshida, K. Kinosita Jr., *Nature* **386**, 299 (1997).
13. R. K. Soong, S. J. Stelick, G. D. Bachand, C. D. Montemagno, *Technical Proceedings of the Second International Conference on Modeling and Simulation of Microsystems*, San Juan, Puerto Rico, 19–21 April 1999 (Computational Publications, Boston, 1999), pp. 95–98.

14. Site-directed mutagenesis was used to (i) change the α initiation codon from ATG to CTG, (ii) change the αCys[193] to Ser, (iii) change the γSer[107] to Cys, (iv) change the γ initiation codon from GTG to ATG, and (v) change the γ termination codon from TAG to TAA in the cloned F_1-ATPase construct (pGEM-DEMH). The construct also contained a 10-histidine tag that was inserted immediately downstream of the β initiation codon. The recombinant protein was expressed in *E. coli* JM103 Δ(*uncB-uncD*) and purified using affinity (i.e., Ni–nitrilotriacetic acid) and size exclusion chromatography.

15. T. Matsui, M. Yoshida, *Biochim. Biophys. Acta* **1231**, 139 (1995).

16. The exposure pattern written on the cover slip consisted of dots with a 5-μm horizontal and vertical pitch and border marks to identify the post region. The dots averaged 50 to 120 nm in diameter, depending on the e-beam exposure dose, which varied from 10 to 30 fC/μm². The exposed area measured 300 μm by 300 μm, exclusive of the border marks. The border marks (lines 50 μm wide) were spaced 0.5 μm from the edge of the post region.

17. The patterning was performed on silicon wafers that were spin-coated with 4% PMMA in methoxybenzene at 3000 rpm, resulting in a thickness of ~150 nm. The width of the nanopropellers was 150 nm; their length varied from 750 nm to 1.4 μm, depending on the exposure dose, which varied from 3.75 to 4.5 nC/cm. The optimum dose was determined to be 4.3 nC/cm.

18. The synthetic His-rich peptide was specifically biotinylated to the NH_2-terminal Cys residue through disulfide linkage in the presence of N,N-dimethylformamide. A 100-μl aliquot of the biotinylated peptide was incubated with 400 μl of the nanopropellers for 15 min, then dialyzed against 1× PBS to remove any excess peptide and biotin maleimide.

19. D. J. Jeffrey, Y. Onishi, *J. Mech. Appl. Math.* **34**, 129 (1981).

20. A. J. Hunt, F. Gittes, J. Howard, *Biophys. J.* **67**, 766 (1994).

21. L. Stryer, *Biochemistry* (Freeman, New York, ed. 4, 1999), pp. 445–447.

22. H. Omote et al., *Proc. Natl. Acad. Sci. U.S.A.* **96**, 7780 (1999).

23. H. Noji et al., *Biochem. Biophys. Res. Commun.* **260**, 597 (1999).

24. T. Hisabori, A. Kondoh, M. Yoshida, *FEBS Lett.* **463**, 35 (1999).

25. We thank F. Peters for figure preparation and assistance in digitization of the data. Supported by grants from the Keck Fellowship Program, Office of Naval Research, and Defense Advanced Research Projects Agency (N00014-99-1-0436CS), NSF (ECS-9007033 and ECS-7876771), U.S. Department of Energy (DE-FG07-96ER14703), and NASA (NAG5-8775).

Mechanisms of Ordering in Striped Patterns

Christopher Harrison,[1] Douglas H. Adamson,[2]
Zhengdong Cheng,[1]* John M. Sebastian,[3]
Srinivasan Sethuraman,[4] David A. Huse,[1] Richard A. Register,[3]
P. M. Chaikin[1]

We have studied the ordering dynamics of the striped patterns of a single layer of cylindrical block copolymer microdomains in a thin film. By tracking disclinations during annealing with time-lapse atomic force microscopy, we observe a dominant mechanism of disclination annihilation involving three or four disclinations (quadrupoles). Pairwise disclination annihilation events are suppressed as a result of the topological constraints in this system. The kinetic scaling laws with exponents observed here are consistent with topologically allowed annihilation events involving multiple disclinations. The results provide insight into two-dimensional pattern formation and may lead to the successful application of block copolymer lithography.

Striped patterns are produced in a variety of disparate systems, including Rayleigh-Benard convection cells, ferrimagnetic films with dipolar interactions, and biological development such as with a zebra's stripes, or perhaps closer at hand, in one's fingerprints (*1*). A classic realization of a nondriven striped system is the two-dimensional (2D) smectic liquid crystal. This system has been the focus of intense research since being discussed by several seminal articles two decades ago (*2*). Although there has been recent progress in understanding equilibrium phenomena such as the role of orientational and translational order in 2D smectics (*3, 4*), little is known about the kinetics and mechanisms by which order evolves in a 2D smectic system after being quenched from the disordered state, although this has been explored

by simulations (*5–8*). The most pressing application for understanding pattern formation in 2D smectics is block copolymer lithography—a process that uses self-assembled patterns (such as single layers of cylinders or spheres) as a template to fabricate devices at the nanometer-length scale (*9–11*). Therefore, our motivation is both fundamental understanding of pattern coarsening and optimization of microdomain order for copolymer lithography, an application that has been used to produce an unprecedented density of metal dots for information storage (*12*), and most recently, to fabricate InGaAs/GaAs quantum dots for laser emission (*13*). We show that the coarsening process is driven by the interaction of topological defects and that the measured kinetic exponents can be understood in terms of a dominant annihilation mechanism that involves more than two disclinations.

Our model system consists of microphase separated block copolymers in thin films. Block copolymers consist of two or more homogeneous but chemically distinct blocks that have been connected with a covalent bond (*14*). Microphase separation produces morphologies largely set by the volume fraction, such as

lamellae, cylinders, or spheres. Although these fundamental morphologies have been well studied for decades, the factors that determine the range of orientational and translational order (grain size) are not well understood. The coarsening kinetics in three dimensions have been studied (*15–17*), but no mechanistic understanding of the ordering process has been developed, partly owing to lack of data on the real-space dynamics during pattern development, which is our focus here.

A polystyrene-polyisoprene (PS-PI) diblock was synthesized by means of living anionic polymerization with masses of 30 and 11 kg/mol for the PS and PI blocks (SI 30-11) to produce PI cylinders in a PS matrix. This diblock was applied to carbon-coated silicon substrates by spin coating from a dilute solution, and order was induced through vacuum annealing (Fig. 1A) (*18*). A representative image from a similar system shows cylinders (lighter) lying parallel to the substrate (Fig. 1B). Because samples sizes were on the order of square centimeters, there were at least 10^5 microdomain repeat spacings in any direction, thereby negating edge effects. After annealing, microdomains were preferentially stained with the vapors of OsO_4 to provide contrast for a Zeiss 982 scanning electron microscope (SEM) (*18–20*). The SEM allowed us to image large areas of the polymer film at high resolution for accurate measurements of the average grain size.

The orientational correlation length (ξ_2) of the pattern was measured as a function of annealing time to quantitatively characterize the degree of microdomain order. This was accomplished by collecting many SEM images of each sample and computationally measuring the local orientational order parameter, $\psi(\vec{r}) = \exp[2i\theta(\vec{r})]$, where $\vec{r}$ is position and θ is the microdomain or stripe orientation (similar to director) (*21*). The azimuthally averaged correlation function $g_2(r) = \langle \psi(0)\psi(r) \rangle$ was then calculated and the correlation length ξ_2 was measured by fitting $g_2(r)$ with e^{-r/ξ_2}. Two annealing temperatures (413 K and 443 K) were examined

[1]Department of Physics, [2]Princeton Materials Institute, [3]Department of Chemical Engineering, Princeton University, Princeton, NJ 08544, USA. [4]Jet Propulsion Laboratory, 4800 Oak Grove Drive, Mailstop 302-306, Pasadena, CA 91109, USA.

*Present address: ExxonMobil Research and Engineering Company, 1545 Route 22 East, Annandale, NJ 08801-0998, USA.